Electronic Supplementary Material (ESI) for Digital Discovery.
This journal is © The Royal Society of Chemistry 2023

Supporting Information: Automatic Mechanism Generation Involving Kinetics of Surface Reactions with Bidentate Adsorbates

Bjarne Kreitz,[*,†,¶] Katrín Blöndal,[†,¶] Kirk Badger,[†] Richard H. West,[‡] and C. Franklin Goldsmith[*,†]

†*School of Engineering, Brown University, Providence, RI 02912, USA*

‡*Department of Chemical Engineering, Northeastern University, Boston, MA 02115, USA*

¶*These authors contributed equally to this work*

E-mail: bjarne_kreitz@brown.edu; franklin_goldsmith@brown.edu

1 Potential energy diagrams

Potential energy diagrams for the `Surface_Bidentate_Dissociation`, `Surface_Dissociation`, and `Surface_Dissociation_to_Bidentate` families are shown in Figures S1 to S3.

2 Raw DFT data

The raw DFT data and results from the vibrational analysis are shown in Table S1.

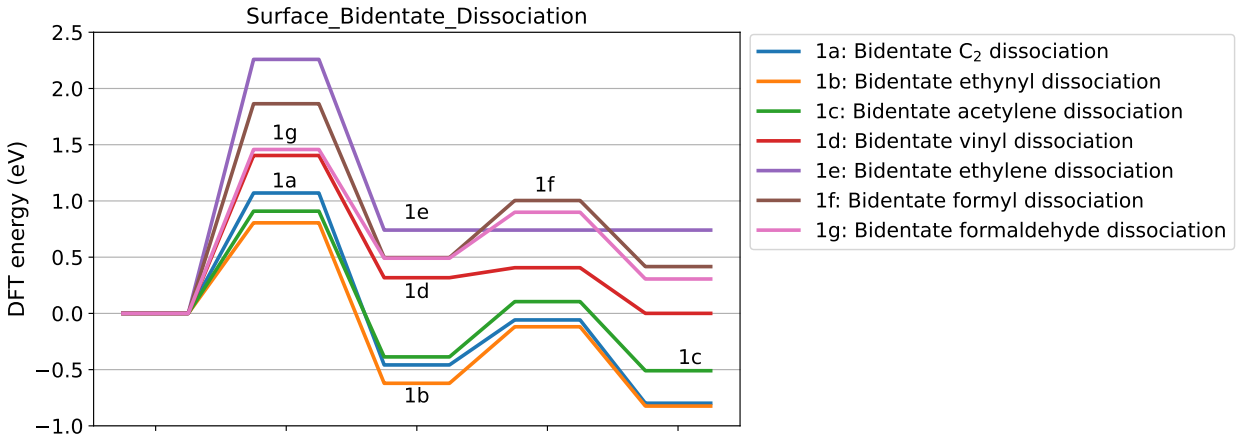

Figure S1: A potential energy diagram for the reactions added to the `Surface_Bidentate_Dissociation` family training reaction database in RMG, showing the (higher) first reaction energy barriers which are listed in Table 1 of the main manuscript, and the subsequent diffusion barriers leading to a more stable final state (if there is one).

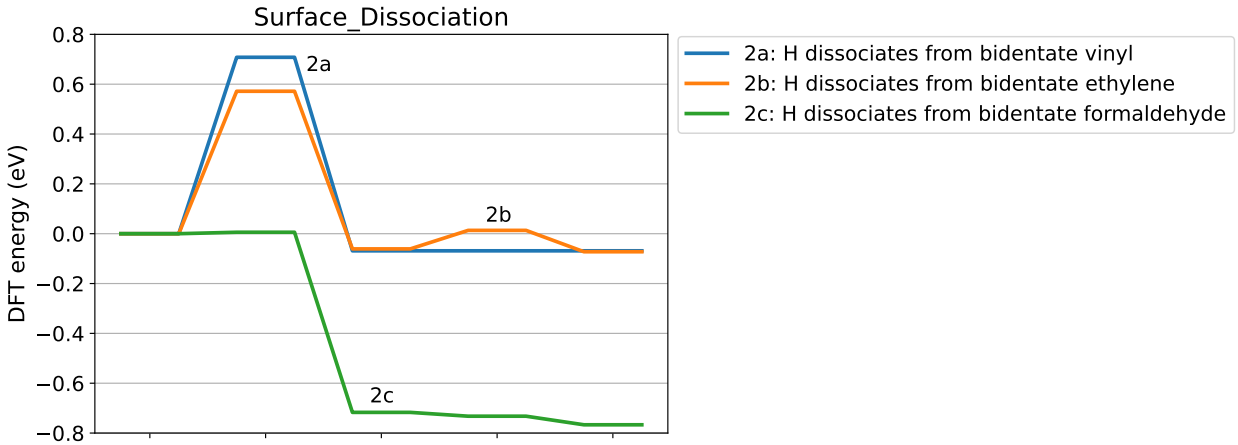

Figure S2: A potential energy diagram for the reactions added to the `Surface_Dissociation` family training reaction database in RMG, showing the (higher) first reaction energy barriers which are listed in Table 1 of the main manuscript, and the subsequent diffusion barrier (2b) and energy decline (2c) leading to a more stable final state.

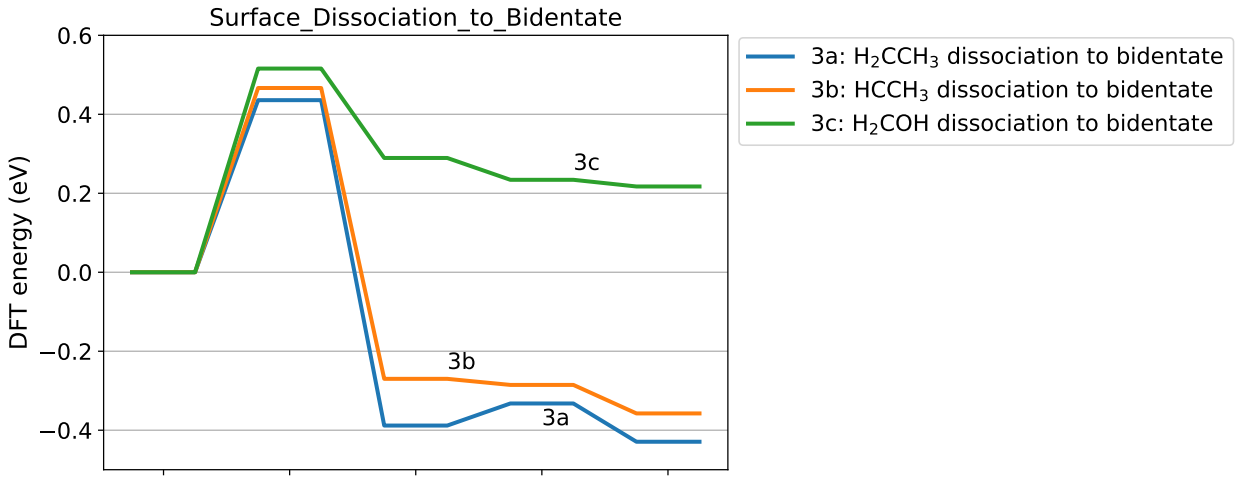

Figure S3: A potential energy diagram for the reactions added to the `Surface_Dissociation_to_Bidentate` family training reaction database in RMG, showing the (higher) first reaction energy barriers which are listed in Table 1 of the main manuscript, and the subsequent diffusion barrier (3a) and energy decline (3b and 3c) leading to a more stable final state.

Table S1: Raw DFT data from the transition state calculation.

Reaction	$E_{\mathrm{SPE}}^{\mathrm{IS}}$(eV)	$E_{\mathrm{ZPE}}^{\mathrm{IS}}$(eV)	ν^{IS}(cm^{-1})	$E_{\mathrm{SPE}}^{\ddagger}$(eV)	$E_{\mathrm{ZPE}}^{\ddagger}$(eV)	$\nu^{\ddagger}$(cm^{-1})
$^{*}C^{*}C \rightleftharpoons {}^{*}C + {}^{*}C$	-119113.925	0.188	224, 321, 390, 396, 442, 1264	-119112.836	0.17	341, 438, 534, 688, 740
$^{*}CH^{*}C \rightleftharpoons {}^{*}CH + {}^{*}C$	-119130.929	0.468	106, 214, 306, 376, 494, 716, 854, 1392, 3098	-119130.106	0.45	317, 464, 535, 622, 704, 768, 863, 2991
$^{*}CH^{*}CH \rightleftharpoons {}^{*}CH + {}^{*}CH$	-119148.290	0.8	263, 298, 318, 534, 608, 752, 824, 961, 1105, 1238, 2991, 3009	-119147.320	0.739	385, 510, 561, 633, 680, 691, 768, 870, 885, 2959, 2978
$^{*}CH^{*}CH_2 \rightleftharpoons {}^{*}CH + {}^{*}CH_2$	-119164.669	1.084	195, 238, 370, 507, 586, 663, 724, 936, 980, 1056, 1103, 1366, 2884, 2921, 2950	-119163.182	1.001	202, 247, 456, 516, 576, 627, 772, 807, 874, 936, 1308, 2899, 2942, 2974
$^{*}CH_2^{*}CH_2 \rightleftharpoons {}^{*}CH_2 + {}^{*}CH_2$	-119181.123	1.405	148, 163, 178, 449, 544, 634, 781, 924, 986, 1037, 1041, 1174, 1376, 1408, 2914, 2921, 2983, 3007	-119178.692	1.232	34, 72, 145, 230, 257, 684, 697, 764, 767, 830, 839, 1321, 1323, 2923, 2923, 3037, 3038
$^{*}CH_2 + {}^{*}CH_2 \rightleftharpoons {}^{*}CH_2^{*}CH_2$	-119180.303	1.325	185, 190, 401, 424, 577, 582, 694, 700, 710, 722, 905, 920, 1333, 1335, 2886, 2886, 2969, 2969	-119178.692	1.232	34, 72, 145, 230, 257, 684, 697, 764, 767, 830, 839, 1321, 1323, 2923, 2923, 3037, 3038
$^{*}CH^{*}O \rightleftharpoons {}^{*}CH + {}^{*}O$	-119411.215	0.485	119, 188, 238, 388, 625, 803, 1182, 1434, 2848	-119409.285	0.419	188, 286, 471, 522, 604, 790, 899, 3000
$^{*}CH + {}^{*}O \rightleftharpoons {}^{*}CH^{*}O$	-119410.752	0.438	310, 330, 399, 451, 468, 582, 778, 780, 2952	-119409.285	0.419	188, 286, 471, 522, 604, 790, 899, 3000
$^{*}CH_2^{*}O \rightleftharpoons {}^{*}CH_2 + {}^{*}O$	-119426.922	0.768	127, 199, 247, 377, 520, 618, 934, 1116, 1143, 1403, 2811, 2889	-119425.391	0.694	92, 183, 377, 423, 456, 655, 759, 901, 1326, 2950, 3068
$^{*}CH_2 + {}^{*}O \rightleftharpoons {}^{*}CH_2^{*}O$	-119426.578	0.73	208, 334, 368, 370, 471, 572, 659, 721, 882, 1331, 2891, 2981	-119425.391	0.694	92, 183, 377, 423, 456, 655, 759, 901, 1326, 2950, 3068
$^{*}CH^{*}CH_2 + {}^{*} \rightleftharpoons {}^{*}CH^{*}CH + {}^{*}H$	-119164.669	1.084	195, 238, 370, 507, 586, 663, 724, 936, 980, 1056, 1103, 1366, 2884, 2921, 2950	-119163.837	0.96	266, 278, 316, 515, 537, 629, 780, 878, 1022, 1131, 1228, 1905, 2995, 3010

Continued on next page ...

Table S1 – continued from previous page

Reaction	E^{IS}_{SPE}(eV)	E^{IS}_{ZPE}(eV)	ν^{IS}(cm^{-1})	$E^{\ddagger}_{SPE}$(eV)	$E^{\ddagger}_{ZPE}$(eV)	$\nu^{\ddagger}$(cm^{-1})
$^{*}CH^{*}CH + {}^{*}H \rightleftharpoons {}^{*}CH^{*}CH_2 + {}^{*}$	-119164.641	0.987	277, 302, 322, 378, 409, 534, 608, 750, 824, 960, 1105, 1237, 2211, 2990, 3008	-119163.837	0.96	266, 278, 316, 515, 537, 629, 780, 878, 1022, 1131, 1228, 1905, 2995, 3010
$^{*}CH_2^{*}CH_2 + {}^{*} \rightleftharpoons {}^{*}CH_2^{*}CH + {}^{*}H$	-119181.123	1.405	148, 163, 178, 449, 544, 634 781, 924, 986, 1037, 1041, 1174, 1376, 1408, 2914, 2921, 2983, 3007	-119180.404	1.257	202, 248, 308, 501, 552, 579, 711, 890, 951, 1017, 1060, 1119, 1377, 1974, 2899, 2907, 2970
$^{*}CH_2^{*}CH + {}^{*}H \rightleftharpoons {}^{*}CH_2^{*}CH_2 + {}^{*}$	-119181.008	1.229	234, 269, 389, 504, 514, 567, 661, 669, 726, 937, 987, 1065, 1086, 1117, 1369, 2882, 2908, 2947	-119180.404	1.257	202, 248, 308, 501, 552, 579, 711, 890, 951, 1017, 1060, 1119, 1377, 1974, 2899, 2907, 2970
$^{*}CH_2^{*}O + {}^{*} \rightleftharpoons {}^{*}CH^{*}O + {}^{*}H$	-119426.922	0.768	127, 199, 247, 377, 520, 618, 934, 1116, 1143, 1403, 2811, 2889	-119426.898	0.75	200, 248, 348, 494, 612, 944, 1107, 1145, 1386, 2726, 2888
$^{*}C^{*}CH_2 + {}^{*} \rightleftharpoons {}^{*}C^{*}CH + {}^{*}H$	-119148.491	0.818	220, 299, 421, 471, 506, 701, 914, 964, 1258, 1403, 2974, 3066	-119146.959	0.608	242, 318, 386, 422, 461, 596, 646, 831, 1300, 1513, 3096
$^{*}C^{*}CH + {}^{*}H \rightleftharpoons {}^{*}C^{*}CH_2 + {}^{*}$	-119147.310	0.598	12, 80, 304, 409, 421, 446, 586, 781, 841, 1245, 1402, 3134	-119146.959	0.608	242, 318, 386, 422, 461, 596, 646, 831, 1300, 1513, 3096
$^{*}CH^{*}CH + {}^{*} \rightleftharpoons {}^{*}C^{*}CH + {}^{*}H$	-119148.315	0.802	259, 299, 314, 536, 602, 751, 828, 965, 1110, 1276, 2990, 3008	-119146.771	0.61	249, 286, 301, 465, 494, 582, 741, 950, 1262, 1456, 3057
$^{*}C^{*}CH + {}^{*}H \rightleftharpoons {}^{*}CH^{*}CH + {}^{*}$	-119147.426	0.638	202, 290, 307, 336, 383, 486, 706, 828, 831, 1321, 1475, 3130	-119146.771	0.61	249, 286, 301, 465, 494, 582, 741, 950, 1262, 1456, 3057
$^{*}CH^{*}CH_2 + {}^{*} \rightleftharpoons {}^{*}C^{*}CH_2 + {}^{*}H$	-119164.695	1.083	204, 239, 374, 507, 572, 661, 721, 936, 982, 1059, 1105, 1366, 2883, 2909, 2948	-119164.134	0.973	209, 291, 407, 484, 504, 631, 727, 928, 987, 1225, 1403, 1871, 2968, 3060

Continued on next page ...

Table S1 – continued from previous page

Reaction	E^{IS}_{SPE}(eV)	E^{IS}_{ZPE}(eV)	ν^{IS}(cm^{-1})	$E^{\ddagger}_{SPE}$(eV)	$E^{\ddagger}_{ZPE}$(eV)	$\nu^{\ddagger}$(cm^{-1})
$^*CH_2CH_3 + 2\,^* \rightleftharpoons {}^*CH^*_2CH_2 + {}^*H$	-119197.158	1.683	88, 95, 126, 245, 246, 473, 671, 884, 912, 1022, 1126, 1194, 1332, 1394, 1401, 1415, 2843, 2887, 2909, 2930, 2955	-119196.588	1.549	73, 157, 176, 271, 420, 563, 644, 805, 986, 1011, 1041, 1124, 1184, 1372, 1396, 2002, 2873, 2903, 2975, 3005
$^*CHCH_3 + 2\,^* \rightleftharpoons {}^*CH^*CH_2 + {}^*H$	-119180.795	1.372	127, 182, 197, 261, 368, 504, 797, 921, 937, 1050, 1222, 1323, 1375, 1386, 2823, 2838, 2897, 2917	-119180.204	1.247	138, 225, 238, 399, 485, 601, 715, 805, 991, 1091, 1101, 1134, 1371, 2070, 2892, 2899, 2965
$^*CH_2OH + 2\,^* \rightleftharpoons {}^*CH^*_2O + {}^*H$	-119443.667	1.103	61, 97, 149, 289, 418, 509, 752, 1024, 1094, 1169, 1338, 1411, 2885, 2993, 3620	-119442.978	0.93	188, 207, 297, 371, 529, 687, 769, 946, 1129, 1137, 1396, 1539, 2858, 2944
$^*CH^*_2O + {}^*H \rightleftharpoons {}^*CH_2OH + 2\,^*$	-119443.295	0.948	82, 182, 264, 354, 371, 391, 521, 624, 940, 1116, 1146, 1398, 2219, 2799, 2892	-119442.978	0.93	188, 207, 297, 371, 529, 687, 769, 946, 1129, 1137, 1396, 1539, 2858, 2944
$^*CCH_3 + 2\,^* \rightleftharpoons {}^*C^*CH_2 + {}^*H$	-119165.229	1.096	151, 153, 168, 401, 456, 460, 952, 953, 1114, 1320, 1386, 1387, 2875, 2948, 2952	-119164.064	0.962	187, 247, 273, 415, 442, 533, 824, 1002, 1013, 1236, 1392, 1942, 2960, 3057
$^*C^*CH_2 + {}^*H \rightleftharpoons {}^*CCH_3 + 2\,^*$	-119164.776	0.953	214, 302, 422, 474, 510, 545, 576, 702, 913, 964, 1061, 1260, 1403, 2971, 3062	-119164.064	0.962	187, 247, 273, 415, 442, 533, 824, 1002, 1013, 1236, 1392, 1942, 2960, 3057
$CH_2CH^*_2 + {}^* \rightleftharpoons {}^*CH^*_2CH_2$	-119180.768	1.412	86, 139, 144, 355, 424, 697, 804, 896, 952, 967, 1176, 1198, 1400, 1471, 2973, 2973, 3051, 3073	-119180.631	1.388	111, 152, 268, 449, 645, 833, 860, 898, 975, 1152, 1180, 1385, 1446, 2962, 2966, 3042, 3068
$^*CHCH_2 + {}^* \rightleftharpoons {}^*CH^*CH_2$	-119163.781	1.061	12, 61, 129, 294, 449, 517, 842, 874, 929, 1177, 1335, 1535, 2952, 2987, 3039	-119163.742	1.054	12, 139, 281, 452, 517, 850, 874, 940, 1184, 1325, 1485, 2944, 2971, 3032

3 Transition State Theory and BEP relations

We calculate the reaction rate constants using canonical transition state theory (TST):

$$k_{TST}(T) = \frac{k_B T}{h} \frac{Q^{\ddagger}}{Q_R} e^{(-E_0/k_B T)}, \tag{1}$$

where $Q^{\ddagger}$ and Q_R are the transition state and reactant partition functions, respectively, and E_0 is the potential energy barrier. In this study, we use the harmonic approximation to obtain the partition functions. RMG uses Arrhenius-type equations for to compute the rate constants. Fitting a regular Arrhenius expression to the rate constants is sufficient over the considered temperature range, which reads as

$$k\,(T) = \frac{A}{\Gamma^{n-1}} e^{(-E_a/RT)} \tag{2}$$

where n is the number of reactants and Γ is the surface site density of the Pt(111) facet, which is determined from the (3×3) unit cell to be $2.39 \times 10^{-9}\,\mathrm{mol\,cm^{-2}}$. Figure S4 shows a comparison of the fitted Arrhenius expressions and the rate constants derived from harmonic transition state theory.

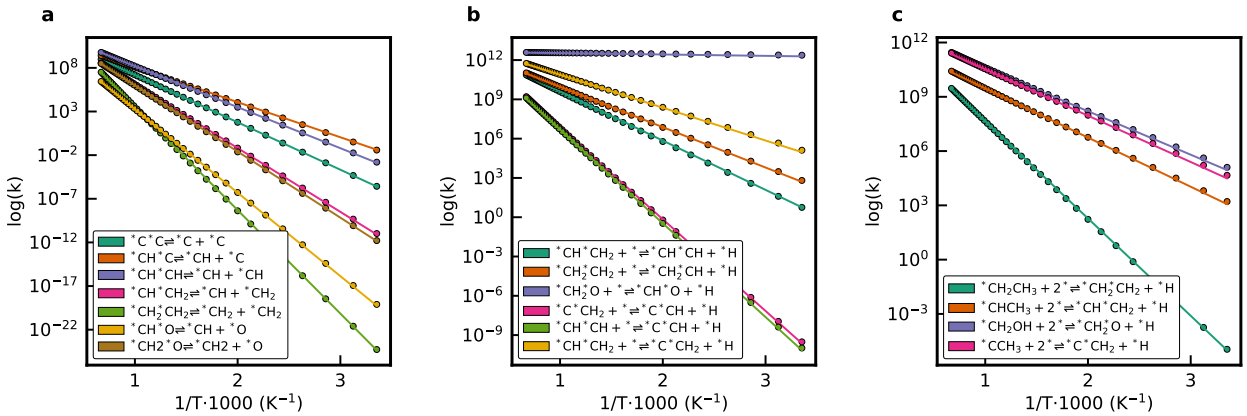

Figure S4: Comparison of the rate constants derived from transition state theory and from the fitted Arrhenius expressions for the a) `Surface_Bidentate_Dissociation`, b) `Surface_Dissociation`, and c) `Surface_Dissociation_to_Bidentate` family.

Brønsted (Bell)-Evans-Polanyi relations[S1] were constructed by grouping the elementary reactions according to their reaction families.

$$E_a = E_0 + \alpha \Delta H_{rxn}, \tag{3}$$

where E_0 is a reference activation energy. The slope α describes the dependence of the activation energy on the reaction enthalpy, and correlates with the position of the transition state along the reaction pathway.

Figure S5 show the rate constants calculated from DFT with the rate constants calculated using a

general rate rule in RMG,

$$k(T) = Ae^{-(E_a^0 + \alpha \Delta H_{rxn})/RT}, \tag{4}$$

for the new and updated reaction families, respectively. BEP plots were used to get values for α and E_a^0, whereas A and n were obtained by fitting to the average rate constant of the respective family. The plots show that while the general rules are relatively close to the TST result for some of the reactions, for others it differs from the TST rate constant results, k_{TST}, by multiple orders of magnitude. This deviation is mostly caused by the uncertainty in the BEP relations of approx. $\pm 30\,\mathrm{kJ\,mol^{-1}}$ due to the scatter of the data points. Therefore, BEP results are useful to obtain a rough estimate of the rate constants for unknown reactions, but it is necessary to perform additional electronic structure calculations to refine the rate constants. All investigated reactions in this work were provided in a reaction library. If RMG finds a reaction in a library, these parameters are prioritized over the general rate rules.

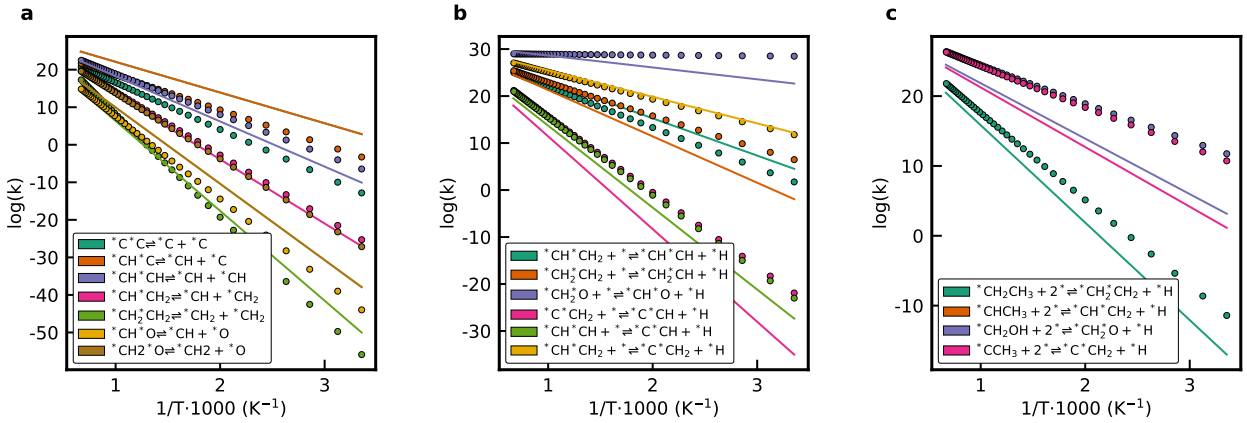

Figure S5: Rate constants from transition state theory and the rate constants calculated with the BEP rules in RMG for the a) `Surface_Bidentate_Dissociation`, b) `Surface_Dissociation`, and c) `Surface_Dissociation_to_Bidentate` family.

Table S2: The modified Arrhenius parameters for the reverse of reactions that are endothermic in the forward direction. In the training reactions database of RMG, $\boldsymbol{A}$ is divided by the surface site density $\Gamma = 2.471 \times 10^{-9}\,\mathrm{mol\,m^{-2}}$.

Rxn label	Reaction	A ($\mathrm{m^2\,mol^{-1}\,s^{-1}}$)	Ea ($\mathrm{kJ\,mol^{-1}}$)
$1e_{rev}$	$^*CH_2 + {}^*CH_2 \rightleftharpoons {}^*CH_2{}^*CH_2$	9.89×10^{23}	154
$1f_{rev}$	$^*CH + {}^*O \rightleftharpoons H{}^*C{}^*O$	6.54×10^{21}	142
$1g_{rev}$	$^*CH_2 + {}^*O \rightleftharpoons {}^*CH_2{}^*O$	2.20×10^{22}	115
$2a_{rev}$	$^*CH{}^*CH + {}^*H \rightleftharpoons {}^*CH{}^*CH_2 + {}^*$	3.68×10^{21}	76
$2b_{rev}$	$^*CH_2{}^*CH + {}^*H \rightleftharpoons {}^*CH_2{}^*CH_2 + {}^*$	6.21×10^{21}	63
$2d_{rev}$	$^*C{}^*CH + {}^*H \rightleftharpoons {}^*C{}^*CH_2 + {}^*$	5.19×10^{19}	34
$2e_{rev}$	$^*C{}^*CH + {}^*H \rightleftharpoons {}^*CH{}^*CH + {}^*$	3.32×10^{21}	62
$3c_{rev}$	$^*CH_2{}^*O + {}^*H \rightleftharpoons {}^*CH_2OH + 2\,{}^*$	8.22×10^{20}	29
$3d_{rev}$	$^*C{}^*CH_2 + {}^*H \rightleftharpoons {}^*CCH_3 + 2\,{}^*$	1.07×10^{22}	72

4 Heat of reaction comparison

Table S3 shows a comparison of the enthalpies of reaction computed from the DFT energies of the initial and most stable final state with the reaction enthalpies from the enthalpies of formation in the RMG database. There are three reasons for the deviation between these two reaction enthalpies. First, the enthalpies of formation are calculated at a low coverage limit at 1/9th mono layer (ML), while the final state has a coverage of 2/9th ML, as both adsorbates are on the same slab. Therefore, these two adsorbates exhibit repulsive interactions. These repulsive interactions decreases the stability and lead to a higher energy configuration. Second, the most stable configuration for the final state is not necessarily the most stable configuration if each adsorbate is on a vacant surface. Third, when we calculate the reaction enthalpy directly from the initial and final state using the zero-point corrected DFT energies, we achieve a cancellation of the DFT errors. Converting these energies first to enthalpies of formation using the adsorption reaction approach described in the work of Blondal et al. does not exploit this error cancellation. Due to all these reasons, we see differences between the reaction enthalpies from RMG and from the DFT energies.

Rxn label	ΔH_{rxn}^{DFT} (kJ mol^{-1})	ΔH_{rxn}^{RMG} (kJ mol^{-1})
Surface_Bidentate_Dissociation		
1a	-77.1	-92.3
1b	-79.5	-91.9
1c	-49.2	-53.4
1d	0.0	-2.1
1e	71.5	67.5
1f	40.1	39.5
1g	29.5	37.2
Surface_Dissociation		
2a	-6.7	0.8
2b	-6.9	19.1
2c	-74.0	-52.8
2d	127.9	115.8
2e	130.0	93.5
2f	44.0	-21.6
Surface_Dissociation_to_Bidentate		
3a	-41.4	-12.8
3b	-34.4	-7.0
3c	20.9	41.0
3d	29.9	44.1
Surface_vdW_to_Bidentate		
4a	-156.1	-172.3
4b	-35.0	-71.2
4c	-44.1	-6.7
Surface_Adsorption_Bidentate		
5a	-255.1	-221.4
5b	-147.5	-118.2
5c	-69.4	-60.8

Rxn label	ΔH_{rxn}^{DFT} (kJ mol^{-1})	ΔH_{rxn}^{RMG} (kJ mol^{-1})
Surface_Monodentate_to_Bidentate		
6a	-148	-128.1
6b	-86	-49.5
6c	6	28.8

Table S3: The heat of reaction ΔH_{rxn} considering the most stable final state, ΔH_{rxn} obtained with RMG database values.

4.1 Mechanism Generation

Table S4 summarizes all the rate rules that were used in RMG for the automated construction of the reaction mechanisms for the non-oxidative dehydrogenation of ethane.

Table S4: Brønsted-Evans-Polanyi relations for the reaction families with an exemplary reaction and the literature source of the relation.

Reaction family	A (cm^2 mol^{-1} s^{-1}) or A (cm^4 mol^{-2} s^{-1}) † or A (s^{-1}) ‡ or A (1) ¶	α / −	E_0 / kJ mol^{-1}	Reference
Dissociation of double bonds in α position		$^*CO + {}^* \rightleftharpoons {}^*C + {}^*O$		
R=R	4.18×10^{21}	0.84	185.1	Wang et al.[S2]
C=O	4.18×10^{21}	0.77	142.8	Sutton and Vlachos[S3]
C-C	4.18×10^{21}	0.72	126.4	Sutton and Vlachos[S3]
Dissociation in α position		$^*CH + {}^* \rightleftharpoons {}^*C + {}^*H$		
R-R	4.18×10^{21}	0.84	185.1	Wang et al.[S2]
C-C	4.18×10^{21}	0.72	126.4	Sutton and Vlachos[S3]
C-O	4.18×10^{21}	0.77	142.8	Sutton and Vlachos[S3]
C-H	4.18×10^{21}	0.57	75.3	Sutton and Vlachos[S3]
O-H	4.18×10^{21}	0.26	73.3	Sutton and Vlachos[S3]
C-OH	4.18×10^{21}	0.58	117.7	Sutton and Vlachos[S3]
C-H (bidentate)	7.25×10^{20}	0.961	93.6	This work
Dissociation in β position		$^*COH + {}^* \rightleftharpoons {}^*CO + {}^*H$		
R-R	4.18×10^{21}	0.84	185.1	Wang et al.[S2]
C-H	4.18×10^{21}	0.58	112.9	Sutton et al.[S4]
O-H	4.18×10^{21}	0.26	73.3	Sutton and Vlachos[S3]
Dissociation in β position forming physisorbed species		$^*COOH + {}^* \rightleftharpoons CO_2^* + {}^*H$		
R-R	4.18×10^{21}	0.58	112.9	Sutton et al.[S4]
C-H	4.18×10^{21}	0.58	112.9	Sutton et al.[S4]
O-H	4.18×10^{21}	0.26	73.3	Sutton and Vlachos[S3]
Dissociation of physisorbed species		$H_2O^* + {}^* \rightleftharpoons {}^*OH + {}^*H$		
R-R	4.18×10^{21}	0.84	185.1	Wang et al.[S2]
H_2O	2.09×10^{21}	0.51	97.5	Wang et al.[S2]
C-OH	4.18×10^{21}	0.58	117.7	Sutton and Vlachos[S3]
C-H	4.18×10^{21}	0.57	75.3	Sutton and Vlachos[S3]

Reaction family	A ($cm^2\,mol^{-1}\,s^{-1}$) or A ($cm^4\,mol^{-2}\,s^{-1}$) † or A (s^{-1}) ‡ or A (1) ¶	α / −	E_0 / kJ mol^{-1}	Reference
C_2H_6	4.18×10^{21}	0.57	75.3	Sutton and Vlachos[S3]
C_2H_4	4.18×10^{21}	0.57	75.3	Sutton and Vlachos[S3]
CH_4	4.18×10^{21}	0.57	75.3	Sutton and Vlachos[S3]
Adsorption of physisorbed species		$CO_2 + {}^* \rightleftharpoons CO_2^*$		
R	0.1¶	0.0	0	
Dissociative adsorption		$CH_4 + 2\,{}^* \rightleftharpoons {}^*CH_3 + {}^*H$		
R	0.1¶	0.69	107.9	Wang et al.[S2]
O-H	0.1¶	0.69	107.9	Wang et al.[S2]
C-H	0.1¶	0.69	107.9	Wang et al.[S2]
H_2	0.1¶	0	5	
C_3H_8	1.19¶	0	33.6	Cushing et al.[S5]
CH_3OH	0.1¶	0.76	107.1	Wang et al.[S2]
Abstraction in α position		${}^*CH_3 + {}^*O \rightleftharpoons {}^*CH_2 + {}^*OH$		
R-R,R	4.18×10^{21}	0.37	99.3	Kreitz et al.[S6]
R-H,R	4.18×10^{21}	0.37	99.3	Kreitz et al.[S6]
C-H,O	4.18×10^{21}	0.94	129.3	Sutton et al.[S7]
O-H,O	4.18×10^{21}	0.65	15.4	Sutton et al.[S7]
C-H,C	4.18×10^{21}	0.37	99.3	Kreitz et al.[S6]
Abstraction in β position		${}^*COH + {}^*O \rightleftharpoons {}^*CO + {}^*OH$		
R-R,R	4.18×10^{21}	0.94	129.3	Sutton et al.[S7]
R-C-H,O	4.18×10^{21}	0.94	129.3	Sutton et al.[S7]
R-O-H,O	4.18×10^{21}	0.65	15.4	Sutton et al.[S7]
Abstraction in β position forming one physisorbed species		${}^*COOH + {}^*O \rightleftharpoons CO_2^* + {}^*OH$		
R-R,R	4.18×10^{21}	0.94	129.3	Sutton et al.[S7]
R-C-H,O	4.18×10^{21}	0.94	129.3	Sutton et al.[S7]
R-O-H,O	4.18×10^{21}	0.65	15.4	Sutton et al.[S7]
Abstraction in β position forming two physisorbed species		${}^*COOH + {}^*OH \rightleftharpoons CO_2^* + H_2O^*$		
R-R,R	4.18×10^{21}	0.68	106.1	Sutton et al.[S7]
R-C-H,OH	4.18×10^{21}	0.68	106.1	Sutton et al.[S7]
R-O-H,OH	4.18×10^{21}	0.02	1.9	Sutton et al.[S7]
Bidentate dissociation		${}^*CH{}^*C \rightleftharpoons {}^*CH + {}^*C$		
R-R,R	1.187×10^{12} ‡	0.842	145.69	This work
Monodentate dissociation to bidentate adsorbate		${}^*CH_2CH_3 + 2\,{}^* \rightleftharpoons {}^*CH_2{}^*CH_2 + {}^*H$		
R-R,R	5.726×10^{29} †	0.082	50.67	This work
Monodentate to bidentate		${}^*CCH_2 + {}^* \rightleftharpoons {}^*C{}^*CH_2$		
R-R,R	1×10^{21}	10.0	0	This work
Physisorbed species to bidentate adsorbate		$CH_2CH_2^* + {}^* \rightleftharpoons {}^*CH_2{}^*CH_2$		
R-R,R	1.838×10^{21}	0	12.20	This work

Coverage dependent thermochemistry

The most abundant surface intermediate during the non-oxidative dehydrogenation of C_2H_6 on the Pt(111) surface is ethylidyne ($^*CCH_3$). It will cover the entire surface and reduces the amount of vacant sites necessary for the reaction. DFT calculations were performed at

varying coverages on a Pt(111) (3×3) surface, starting with 1/9th monolayer, which is the reference coverage to 5/9 of $^{*}CCH_3$ coverage. These electronic structure calculations were performed as part of a previous project using the BEEF−vdW functional, which is consistent with the thermophysical values in the RMG database. For details on the DFT calculations, the interested reader is referred to.[S8] Due to repulsive lateral self-interactions, the enthalpy of formation $\Delta_f H$ decreases strongly with increasing coverage Θ as seen in Figure S6.

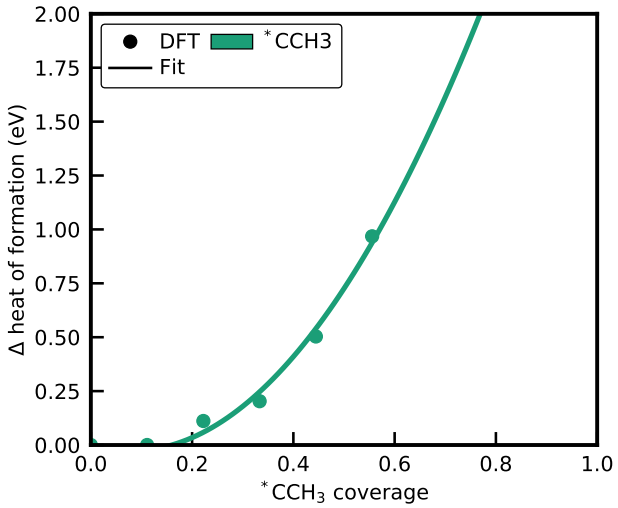

Figure S6: Coverage dependence of the enthalpy of formation of $^{*}CCH_3$ as a function of its own coverage on Pt(111).

In order to subject the enthalpy of formation with a coverage dependence to account for this behavior, a second-order polynomial was fitted to the data. The polynomial reads as

$$\Delta_f H_{^{*}CCH_3} = \Delta_f H^{ref}_{^{*}CCH_3} + a\Theta_{^{*}CCH_3} + b\Theta^2_{^{*}CCH_3} \tag{5}$$

where a and b are the fitted parameters and amount to $a = -0.683\,\text{eV}$ and $b = 4.269\,\text{eV}$, respectively. The effect of coverage on the entropy or heat capacity was neglected, as this effects the stability to a minor extent.

Convergence Study

Figure S7 shows the results from the convergence study, which was used to finalize the termination rate ratio.

Additional Simulation Results

Figure S8 shows the simulations results without the addition of a coverage dependent enthalpy of formation of $^{*}CCH_3$. The results from the reaction path analysis at the entrance of the reactor are displayed in Figure S9.

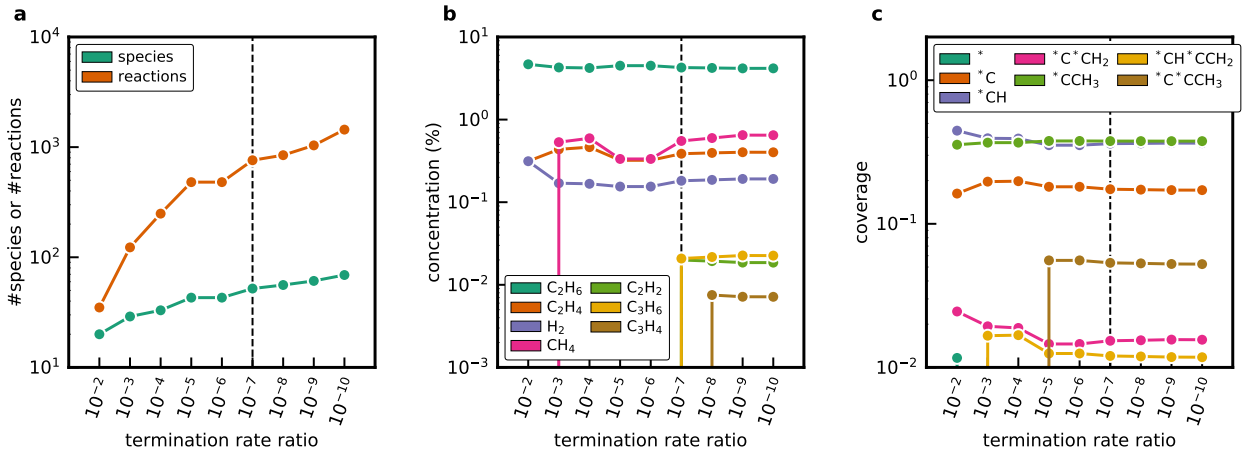

Figure S7: Convergence study to determine the termination rate ratio for the mechanism generation in RMG. The final termination rate ratio is 1×10^{-7}. a) Mechanism metrics. b) Simulated end-of-pipe concentrations and c) simulated coverages at the end of the reactor obtained from the coverage dependent microkinetic models.

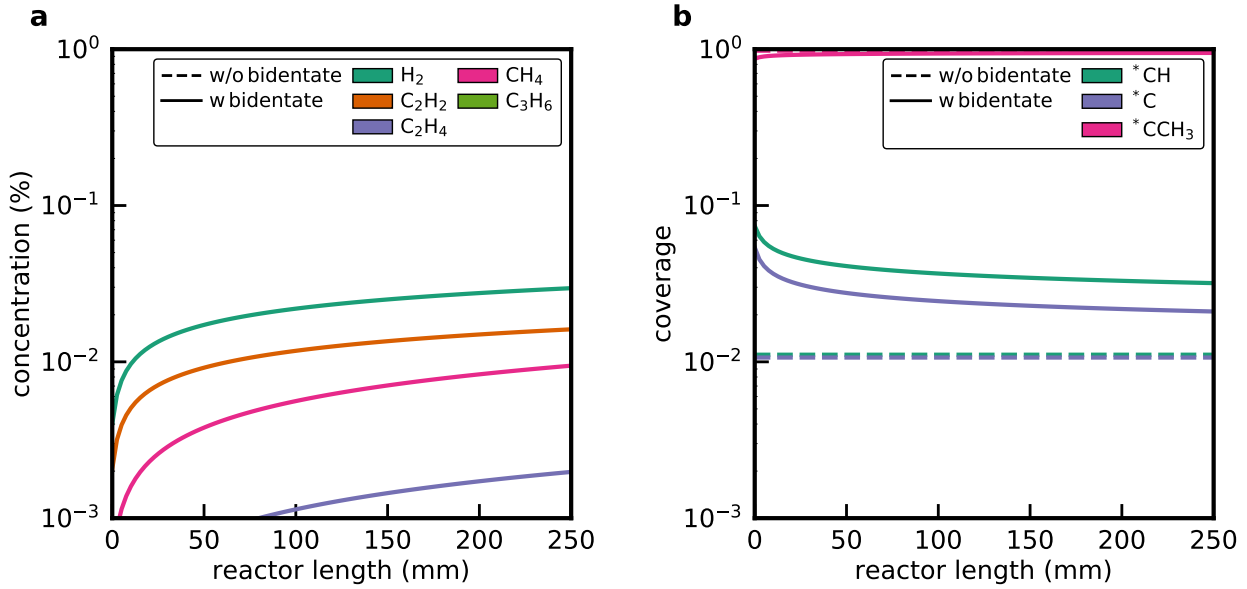

Figure S8: Results from the reactor simulations without coverage dependent enthalpy of formation of $^*CCH_3$ for a) gas-phase concentration profiles and b) surface coverages.

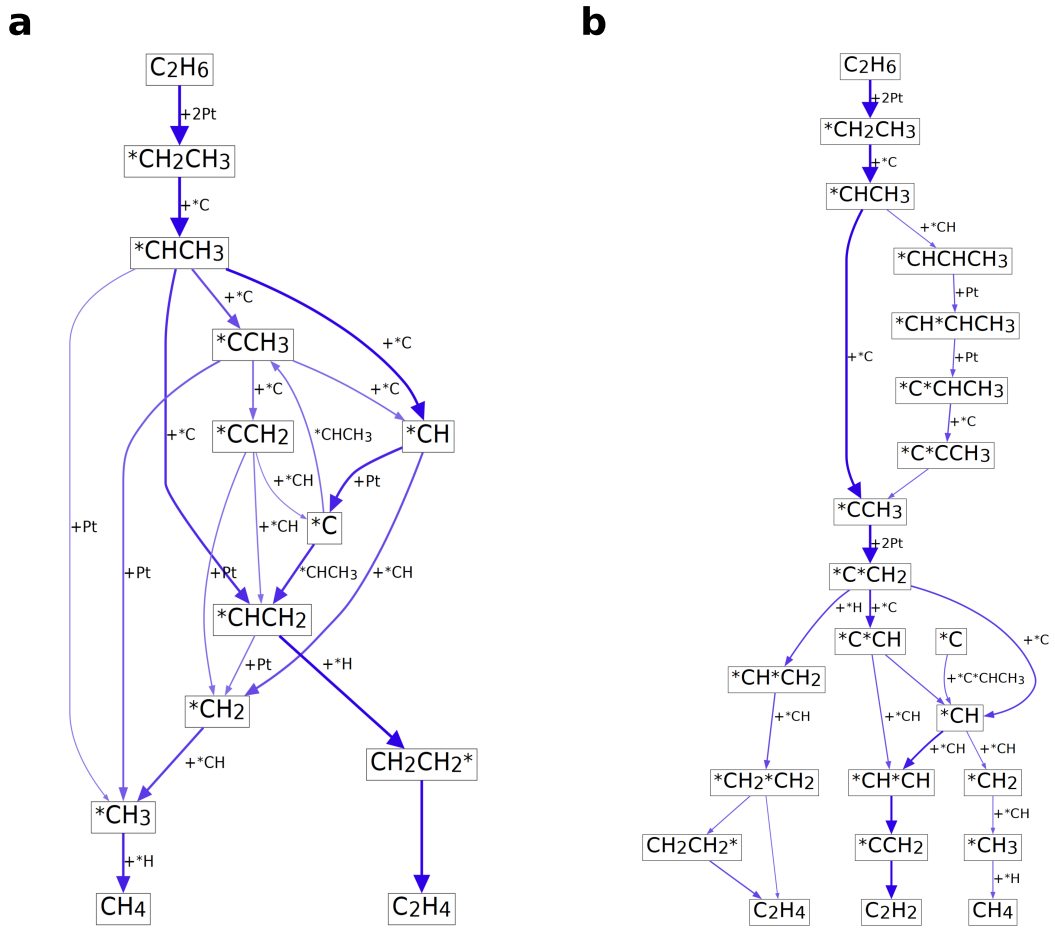

Figure S9: Reaction path analysis at the inlet of the reactor for a) the mechanism generated without bidentate functionalities and b) with the new bidentate features.

Screening Across the Periodic Table with RMG

Linear Scaling Relations for Bidentate Adsorbates in RMG

One of the big advantages of RMG is that we can scale across the periodic table and build a microkinetic model for every point in the descriptor space. This approach is more sophisticated than using a static mechanism since the kinetically relevant pathways can change. As RMG is extended to provide reliable predictions for reactions involving multidentate adsorbates on the reference metal Pt, appropriate scaling relations need to be in place, so they can be extrapolated to other metals with a degree of confidence. Therefore, we performed a study to confirm the suitability of the implemented scaling relations in RMG for polydentate species. RMG uses linear scaling relations (LSRs) to efficiently extrapolate database values to a range of hypothetical metal surfaces without additional DFT calculations.[S9] It has been shown that the adsorption energies of H-containing molecules of C/O/S/N on transition metal surfaces scale linearly with the adsorption energy of the surface adatom:[S10]

$$E_b^{AH_x} = \gamma E_b^A + \xi, \tag{6}$$

where $E_b^{AH_x}$ is the adsorbate binding energy, E_b^A is the binding energy of the reference adatom through which the adsorbate binds, and the intercept ξ is the independent of the metal in question, but unique for each adsorbate. d The proportionality constant γ is a function of the normalized bond order x:

$$\gamma = \frac{x_{\max} - x}{x_{\max}}. \tag{7}$$

Here, $x_{\max}$ is the maximum number of atoms that can bind to the central atom A, and x is the number of bonds of the reference adatom, excluding its bond to the surface site. In other words, the binding energy of an adsorbate on different surfaces scales with normalized bond order. A binding energy scaling relation exists for bidentate adsorbates as well, where for bound molecular fragments B and C within an adsorbate:[S11?]

$$E_b^{B^*-C^*} = \gamma^B E_b^B + \gamma^C E_b^C + \xi^{B^*-C^*}. \tag{8}$$

In Equation (8), it is assumed that the electron interaction at each binding site can be treated separately depending on the bond order at each site, hence the overall bond strength is a sum of the individual scaling terms. Furthermore, this assumption allows for straightforward further generalization for multidentate adsorption beyond two binding sites.[?] RMG uses a consequence of equation 8 to scale binding energies to other metals. In the case of bidentate adsorbates:

$$E_b^{B^*-C^*-M2} = E_b^{B^*-C^*-Pt} + \gamma^B(E_b^{B-M2} - E_b^{B-Pt}) + \gamma^C(E_b^{C-M2} - E_b^{C-Pt}), \tag{9}$$

where M2 represents the second metal. In order to validate the scaling relations in RMG, we

conducted DFT calculations for a various bidentate adsorbates on a range of metals. DFT calculations were performed for all H/C/O-containing bidentates with two heavy atoms on Ag(111), Pd(111), Au(111), Co(0001), Ru(0001), Ni(111), Au(111), Pt(111), Cu(111), Ir(111) and Rh(111). Lattice constants were optimized for every metal. Spin-polarized calculations were conducted for Co(0001) and Ni(111). The workflow for the geometry optimization is identical to the one described in the main manuscript.

The scaling behaviour of the bidentate adsorbates was studied and intercepts ξ were calculated for each adsorbate, using the reference adatom binding energies present in the RMG database. The results were averaged to obtain a general ξ for each adsorbate across the ten metals. The DFT binding energies of the five C/H-containing bidentate adsorbates are plotted vs the carbon adatom binding energies on each metal in Figure S10.

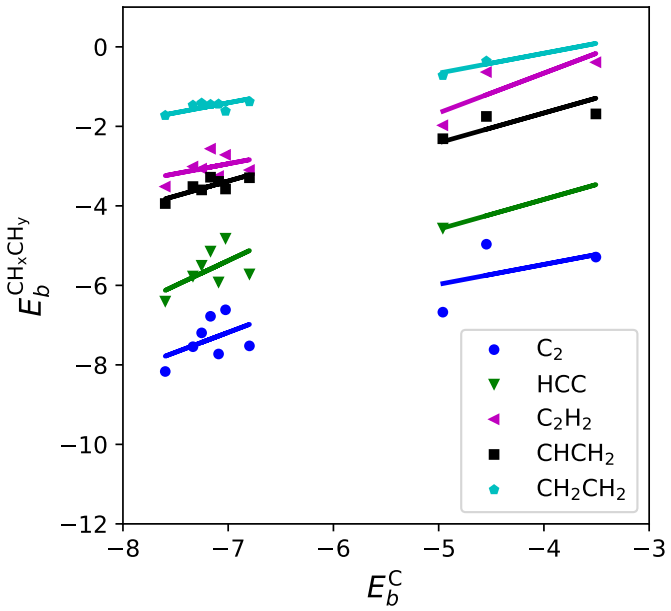

Figure S10: Binding energies E_b of bidentate $^*CH_x^*CH_y$ (x,y=0,1,2) adsorbates versus a C atom binding energy on 10 monometallic transition metal surfaces. The solid lines represent fits to the data for each adsorbate in the respective binding energy region.

The linear scaling fits are included in the plot as solid lines. The plot reveals two carbon binding energy regions, as has previously been observed in Ref.[?] On one hand there is a region with stronger (<−6 eV) carbon atom binding on Pt(111), Pd(111), Ni(111), Ir(111), Rh(111), Ru(0001), and Co(0001), and on the other, a region with weaker binding energy (>−5 eV) for Cu(111), Ag(111), and Au(111). The fittings were performed separately for each of the regions. In the case of $^*C^*C$, $^*C^*CH$ and $^*CH^*CH$, the fits can have different slopes due to multiple possible values of γ resulting from different resonance structures. Bidentate $^*C^*CH$ is not stable on Ag(111) and Au(111). Additionally, a stable $^*CH_2^*CH_2$ configuration on the Ag(111) surface was not found. The value of γ that produced the fit with the lowest mean absolute error (MAE) for each adsorbate in each region was chosen.

The LSR assumption for bidentate adsorbates was then tested by plotting the binding energy resulting from the linear scaling fits against the corresponding DFT results for all seven bidentate adsorbates on all ten metals (see Figure S11). The overall mean absolute error (MAE) is 0.23 eV, which is on the same order of magnitude as the DFT functional error. Highest errors are obtained for *C*C, and the LSRs perform better for the other species (leaving *C*C out gives an MAE of 0.19 eV). In the case of Ag and Au, only monodentate *CCH was found from the DFT geometry relaxation, and therefore *C*CH–Ag(111) and *C*CH–Au(111) are not part of the study. This result shows that it is possible to apply LSR with the implementation in RMG [S9] when building mechanisms that involve bidentate species automatically with RMG and achieve an acceptable accuracy of the thermophysical properties.

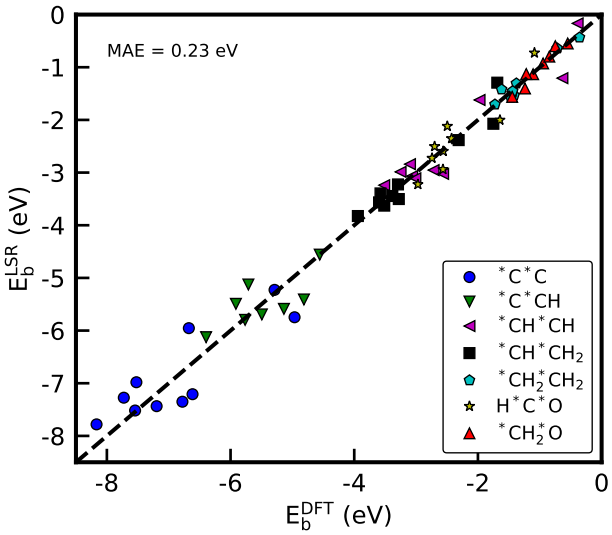

Figure S11: The linear scaling result versus the DFT binding energy for the seven adsorbates on 10 monometallic transition metal surfaces. Enthalpies of formation and DFT binding energies of the adsorbates are strongly correlated and they both show the same trends, which is why only DFT binding energies are shown in this figure.

Linear Scaling Results

The binding energies for *C and *H for all (111) facets used for the linear scaling study are summarized in Table S5. Binding energies for the monometallic facets are provided in the RMG database and it is possible to call the metal in the RMG input file via, e.g., `metal="Pd111"`. The list of these binding energies was compiled using Quantum Espresso and the PBE functional with D3 dispersion corrections. For the bimetallic alloys, relaxed structures were taken from Catalysis-Hub, [S12] which are from the work of Hansen et al. [S13] These structures are 2×2×4 unit cells of the alloys, so the coverage of the adsorbates is 1/4 mono layer. DFT calculations were performed with these structures using identical DFT settings as were used for the compilation of the metal library. Calculations were also performed with an available Pt(111) structure as a reference. The binding energies of *C

and *H obtained for the 2×2 Pt(111) unit cell differ slightly from the results in the metal database with differences of $\Delta E_b^{*C} = 0.042\,\text{eV}$ and $\Delta E_b^{*H} = 0.046\,\text{eV}$. These small differences are probably caused by the higher coverage of the adsorbates and differences in the lattice constant due to different DFT functionals. In order to not artificially skew the results, the binding energies of the alloys were shifted by this difference to align them with the binding energies in the metal database.

Table S5: Summary of the DFT results from the calculations with Quantum ESPRESSO for the adsorbates on Pt(111). The single-point energies (SPE) and zero-point energies (ZPE), as well as the vibrational frequencies for the most stable position, are provided.

Metal	E_b^{*C} (eV)	E_b^{*H} (eV)	$\Gamma\,(\text{mol}\,\text{cm}^{-2})$	core		edge	
				Species	Reactions	Species	Reactions
Ag	-3.506	-2.105	2.292×10^{-9}	19	26	15	39
Au	-4.546	-2.208	2.270×10^{-9}	23	67	21	70
Co	-7.091	-3.020	3.118×10^{-9}	35	2423	26	421
Cu	-4.960	-2.583	2.943×10^{-9}	23	67	21	70
Ir	-7.252	-2.676	2.587×10^{-9}	41	377	22	459
Ni	-6.797	-2.892	3.148×10^{-9}	50	662	14	461
Pd	-7.167	-2.922	2.534×10^{-9}	48	623	16	460
Pt	-7.025	-2.753	2.483×10^{-9}	52	760	19	434
Rh	-7.334	-2.830	2.656×10^{-9}	39	356	23	454
Ru	-7.597	-2.851	2.630×10^{-9}	32	226	28	346
Pd_3In	-6.210	-2.833	2.315×10^{-9}	62	1137	14	483
Pt_3In	-7.001	-2.857	2.317×10^{-9}	49	626	15	460
Pt_3Sn	-6.436	-2.755	2.303×10^{-9}	64	1236	13	589
Pt_3Zn	-7.135	-2.805	2.471×10^{-9}	44	456	18	460

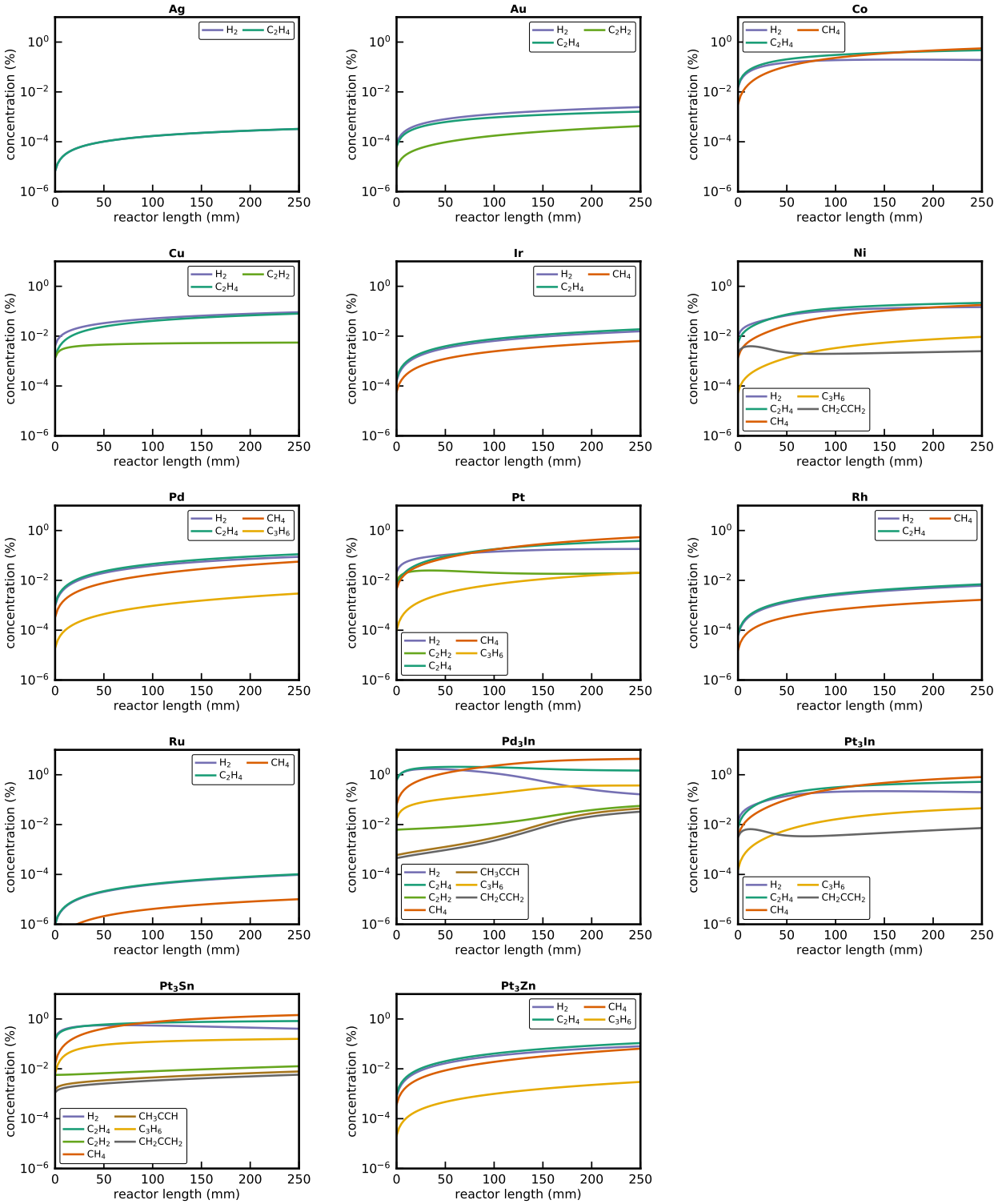

Figure S12: Simulated concentrations profiles along the reactor length for all investigate close-packed metal surfaces at a temperature of 873 K.

References

(S1) Evans, M. G.; Polanyi, M. Inertia and driving force of chemical reactions. *Trans. Far. Soc.* **1938**, *34*, 11–24.

(S2) Wang, S.; Petzold, V.; Tripkovic, V.; Kleis, J.; Howalt, J. G.; Skúlason, E.; Fernández, E. M.; Hvolbæk, B.; Jones, G.; Toftelund, A.; Falsig, H.; Björketun, M.; Studt, F.; Abild-Pedersen, F.; Rossmeisl, J.; Nørskov, J. K.; Bligaard, T. Universal transition state scaling relations for (de)hydrogenation over transition metals. *Phys. Chem. Chem. Phys.* **2011**, *13*, 20760–20765.

(S3) Sutton, J. E.; Vlachos, D. G. Ethanol Activation on Closed-Packed Surfaces. *Ind. Eng. Chem. Res.* **2015**, *54*, 4213–4225.

(S4) Sutton, J. E.; Vlachos, D. G. A Theoretical and Computational Analysis of Linear Free Energy Relations for the Estimation of Activation Energies. *ACS Catal.* **2012**, *2*, 1624–1634.

(S5) Cushing, G. W.; Navin, J. K.; Donald, S. B.; Valadez, L.; Johánek, V.; Harrison, I. C−H Bond Activation of Light Alkanes on Pt(111): Dissociative Sticking Coefficients, Evans−Polanyi Relation, and Gas−Surface Energy Transfer. *J. Phys. Chem. C* **2010**, *114*, 17222–17232.

(S6) Kreitz, B.; Sargsyan, K.; Blöndal, K.; Mazeau, E. J.; West, R. H.; Wehinger, G. D.; Turek, T.; Goldsmith, C. F. Quantifying the Impact of Parametric Uncertainty on Automatic Mechanism Generation for CO_2 Hydrogenation on Ni(111). *JACS Au* **2021**, *1*, 1656–1673.

(S7) Sutton, J. E.; Panagiotopoulou, P.; Verykios, X. E.; Vlachos, D. G. Combined DFT, Microkinetic, and Experimental Study of Ethanol Steam Reforming on Pt. *J. Phys. Chem. C* **2013**, *117*, 4691–4706.

(S8) Kreitz, B.; Lott, P.; Bae, J.; Blöndal, K.; Angeli, S.; Ulissi, Z. W.; Studt, F.; Goldsmith, C. F.; Deutschmann, O. Detailed Microkinetics for the Oxidation of Exhaust Gas Emissions through Automated Mechanism Generation. *ACS Catal.* **2022**, *12*, 11137–11151.

(S9) Mazeau, E.; Satpute, P.; Blöndal, K.; Goldsmith, F.; West, R. Automated Mechanism Generation Using Linear Scaling Relationships and Sensitivity Analyses Applied to Catalytic Partial Oxidation of Methane. *ACS Catal.* **2021**, *11*, 7114–7125.

(S10) Abild-Pedersen, F.; Greeley, J.; Studt, F.; Rossmeisl, J.; Munter, T. R.; Moses, P. G.; Skúlason, E.; Bligaard, T.; Nørskov, J. K. Properties of Adsorption Energies for Hydrogen-Containing Molecules on Transition-Metal Surfaces. *Phys. Rev. Lett.* **2007**, *99*, 016105.

(S11) Jones, G.; Studt, F.; Abild-Pedersen, F.; Nørskov, J. K.; Bligaard, T. Scaling relationships for adsorption energies of C_2 hydrocarbons on transition metal surfaces. *Chem. Eng. Sci.* **2007**, *66*, 6318–6323.

(S12) Winther, K. T.; Hoffmann, M. J.; Boes, J. R.; Mamun, O.; Bajdich, M.; Bligaard, T. Catalysis-Hub.Org, an Open Electronic Structure Database for Surface Reactions. *Sci. Data* **2019**, *6*, 75.

(S13) Hansen, M. H.; Nørskov, J. K.; Bligaard, T. First Principles Micro-Kinetic Model of Catalytic Non-Oxidative Dehydrogenation of Ethane over Close-Packed Metallic Facets. *J. Catal.* **2019**, *374*, 161–170.